NANO LETTERS
Letter
Cite This: *Nano Lett.* 2018, 18, 7372−7377
pubs.acs.org/NanoLett

Oxygen Vacancy Engineering Promoted Photocatalytic Ammonia Synthesis on Ultrathin Two-Dimensional Bismuth Oxybromide Nanosheets

Xiaolan Xue,[†] Renpeng Chen,[†] Hongwei Chen,[†] Yi Hu,[†] Qingqing Ding,[‡] Ziteng Liu,[†] Lianbo Ma,[†] Guoyin Zhu,[†] Wenjun Zhang,[†] Qian Yu,[‡] Jie Liu,[†,§] Jing Ma,[†] and Zhong Jin*[,†]

[†]Key Laboratory of Mesoscopic Chemistry of MOE, School of Chemistry and Chemical Engineering, Nanjing University, Nanjing, Jiangsu 210023, China

[‡]Center of Electron Microscopy and State Key Laboratory of Silicon Materials, Department of Materials Science and Engineering, Zhejiang University, Hangzhou 310027, China

[§]Department of Chemistry, Duke University, Durham, North Carolina 27708, United States

Supporting Information

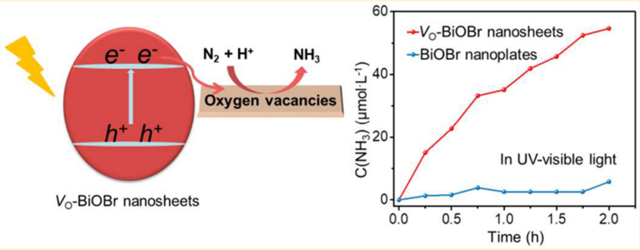

ABSTRACT: The catalytic conversion of nitrogen to ammonia is one of the most important processes in nature and chemical industry. However, the traditional Haber-Bosch process of ammonia synthesis consumes substantial energy and emits a large amount of carbon dioxide. Solar-driven nitrogen fixation holds great promise for the reduction of energy consumption and environmental pollution. On the basis of both experimental results and density functional theory calculations, here we report that the oxygen vacancy engineering on ultrathin BiOBr nanosheets can greatly enhance the performance for photocatalytic nitrogen fixation. Through the addition of polymetric surfactant (polyvinylpyrrolidone, PVP) in the synthesis process, V_O-BiOBr nanosheets with desirable oxygen vacancies and dominant exposed {001} facets were successfully prepared, which effectively promote the adsorption of inert nitrogen molecules at ambient condition and facilitate the separation of photoexcited electrons and holes. The oxygen defects narrow the bandgap of V_O-BiOBr photocatalyst and lower the energy requirement of exciton generation. In the case of the specific surface areas are almost equal, the V_O-BiOBr nanosheets display a highly improved photocatalytic ammonia production rate (54.70 μmol·g^{-1}·h^{-1}), which is nearly 10 times higher than that of the BiOBr nanoplates without oxygen vacancies (5.75 μmol·g^{-1}·h^{-1}). The oxygen vacancy engineering on semiconductive nanomaterials provides a promising way for rational design of catalysts to boost the rate of ammonia synthesis under mild conditions.

KEYWORDS: *Photocatalytic nitrogen fixation, oxygen vacancies engineering, defect and bandgap modulation, ultrathin bismuth oxybromide nanosheets*

Ammonia is one of the most highly produced chemicals in the chemical industry that can serve as a vital precursor for the synthesis of many nitrogenous compounds, especially nitrogen fertilizers.[1] Although nitrogen accounts for 78% of the total volume of the Earth's atmosphere, the fixation of nitrogen to ammonia under mild conditions remains a grand challenge, owing to the strong and nonpolar N−N triple bond (with bond energy of 945 KJ·mol^{-1}) that makes the nitrogen molecules extremely stable and inert.[2−5] The traditional Haber-Bosch method for ammonia synthesis is operated at a high temperature of 300−500 °C and a high pressure of 15−25 MPa,[6,7] undergoing the drawbacks of high energy input and severe environmental impacts.[8,9] Therefore, it is highly desirable to develop a new strategy to synthesize ammonia with less power consumption and more environmentally friendly process. Notably, the nitrogen-fixing bacteria in nature can carry out the process of nitrogen fixation at room temperature and ambient pressure.[10,11] Inspired by the natural photosynthesis using sunlight as the driven force, photocatalytic ammonia synthesis has attracted growing research attention. The photocatalytic nitrogen reduction in the TiO_2 system was first reported by Schrauzer.[12] Subsequently, many efforts had been devoted to improve the nitrogen fixation performance of TiO_2-based photocatalysts by the doping of other elements (e.g., Fe) and the assistance of noble metal (such as Os, Ru, Pt).[13−17] However, the efficiency of photocatalytic dinitrogen reduction is usually low, owing to the easy recombination of photoinduced electrons and holes, the weak adsorption of inert dinitrogen molecules on the

Received: September 9, 2018
Revised: September 30, 2018
Published: October 12, 2018

DOI: 10.1021/acs.nanolett.8b03655
Nano Lett. 2018, 18, 7372−7377

surface of catalysts and the multielectron nature of the reaction.[18,19] Theoretical analysis and experimental efforts indicate that oxygen vacancies in photocatalysts with abundant localized electrons are conducive to adsorb and activate different target molecules and also can promote electron−hole separation and reduce the energy barrier for interfacial charge transfer.[20−24] Some recent studies show that the introduction of nitrogen, oxygen, or sulfur vacancies into catalysts can contribute to the photochemical dinitrogen reduction reaction.[25−29] However, so far the controlled introduction of specific defects in nanostructural materials is still difficult, hence it is very desirable to explore facile and universal strategies for the construction of superior photocatalysts with favorable atomic vacancies and enhanced performance.

Bismuth oxybromide (BiOBr) is a layered ternary oxyhalide semiconductor with the crystalline structure consists of $[Bi_2O_2]^{2+}$ slabs intercalated by the double slabs of Br^- ions stacked along the *z*-direction (Figure 1). Recently, BiOBr nanocrystals has attracted rising attention due to its remarkable photocatalytic performance in visible light range.[30−33] In this study, we present that oxygen vacancy engineering on ultrathin BiOBr nanosheets can significantly improve the performance of photocatalytic nitrogen fixation. The preparation of BiOBr nanosheets with major exposed {001} facets and abundant oxygen vacancies (V_O-BiOBr nanosheets) is controlled by adding a certain amount of polyvinylpyrrolidone (PVP) surfactant during the synthesis process. The as-prepared products in the presence and absence of oxygen vacancies are named as V_O-BiOBr nanosheets and BiOBr nanoplates, respectively. Detailed characterizations and tests confirm that the formation of oxygen vacancies in the crystal lattices of V_O-BiOBr nanosheets can effectively narrow the bandgap, enhance the light absorption, and facilitate the separation of photoinduced electrons and holes. Moreover, density functional theory (DFT) calculations also reveal the energetically favorable adsorption of N_2 molecules on the surface of V_O-BiOBr nanosheets. Therefore, compared to the BiOBr nanoplates without oxygen vacancies, the V_O-BiOBr nanosheets can greatly boost the reaction rate of photocatalytic ammonia synthesis, even in pure water and without any sacrificial reagent.

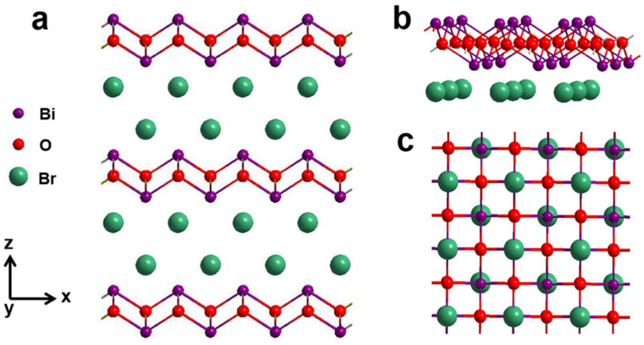

Figure 1. Schematic diagrams of the laminar crystalline structure of BiOBr. (a) The front view, (b) the side view, and (c) the top view of BiOBr crystal unit cells.

The V_O-BiOBr nanosheets and BiOBr nanoplates were synthesized via a facile hydrothermal process at 160 °C, as detailed in the Experimental Section of Supporting Information. Scanning electron microscopy (SEM) and transmission electron microscopy (TEM) were used to characterize the morphological features of the products. Figure 2a shows that the V_O-BiOBr nanosheets consist of large-scale laminar nanosheets. TEM images further reveal its sheetlike structure and rough surface with a thickness of 4−8 nm (Figure 2b). The high-resolution TEM (HRTEM) image in Figure 2c shows that the lattice fringes of V_O-BiOBr nanosheets with a lattice spacing of 0.277 nm, corresponding to the (110) planes of tetragonal BiOBr. Additionally, it can be found that there are crystalline boundaries and defects in the HRTEM image of V_O-BiOBr nanosheets, which is ascribed to the abundant and broadly distributed oxygen vacancies in the V_O-BiOBr nanosheets. As shown in the inset of Figure 2c, the corresponding fast Fourier transform (FFT) pattern shows a regular pattern, suggesting the single-crystalline characteristic of V_O-BiOBr nanosheets. The diffraction spots were recorded along the [001] direction. The angle of 45° in FFT pattern is in good agreement with the theoretical value of the angle between (200) and (110) planes. In contrast, the BiOBr nanoplates exhibit a disklike morphology and flat surface, with an average size of ∼200 nm and thickness of around 15 nm, as depicted in Figure 2d,e. the HRTEM image of BiOBr nanoplates presents a sharp lattice stripes with a *d*-spacing of 0.277 nm (Figure 2f), which is comparable with that of V_O-BiOBr-nanosheets, but with much better crystallinity and uniform contrast, which indicates the ordered single-crystalline structure and fewer defects in BiOBr nanoplates.

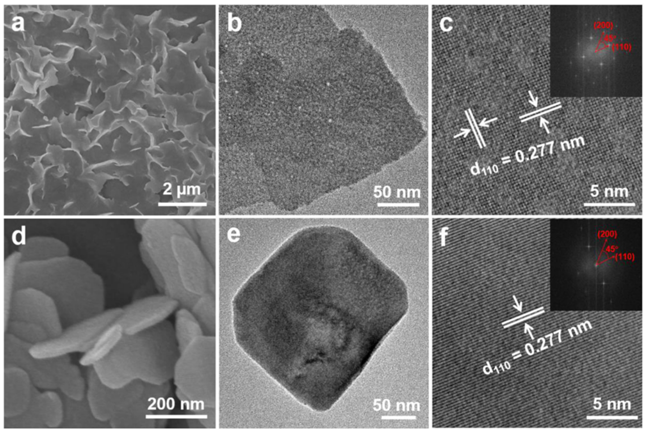

Figure 2. (a,d) SEM images, (b,e) TEM images, (c,f) HRTEM images of the V_O-BiOBr nanosheets and BiOBr nanoplates, respectively.

The crystallographic structures of the as-synthesized samples were also characterized by XRD analysis. As shown in Figure 3a, the XRD peaks of both V_O-BiOBr nanosheets and BiOBr nanoplates can be well assigned to the tetragonal phase BiOBr (JCPDS No. 09-0393). The peak sharpness and relative intensity of V_O-BiOBr nanosheets are much lower than those of BiOBr nanoplates, mainly owing to the oxygen vacancies in V_O-BiOBr nanosheets. More specifically, in the case of V_O-BiOBr nanosheets the intensity ratio of the (110) facet to (001) facet was 2.5, which was smaller than of BiOBr nanoplates (around 3.9). This indicates a preferred (001) orientation in the V_O-BiOBr nanosheets, which is in accordance with the HRTEM results. The possible reason is that during the nucleation process, the negatively charged −C═O bonds of PVP surfactant molecules tend to bind with the unsaturated and positively charged Bi atoms on the BiOBr surface in order to reduce the surface energy, leading to the

DOI: 10.1021/acs.nanolett.8b03655
Nano Lett. 2018, 18, 7372−7377

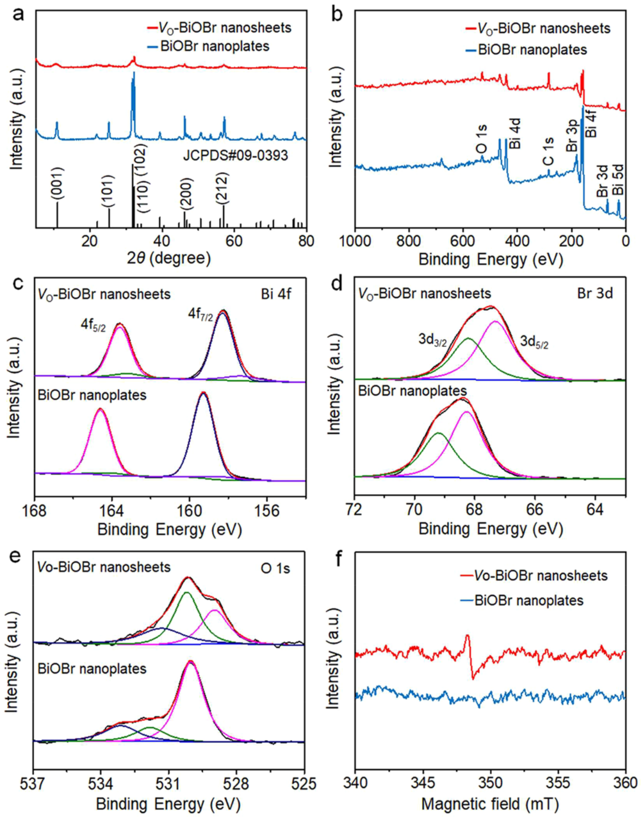

Figure 3. (a) XRD patterns, (b) survey XPS spectra of V_O-BiOBr nanosheets and BiOBr nanoplates, respectively. (c−e) High-resolution XPS scans of (c) Bi 4f, (d) Br 3d, and (e) O 1s regions of V_O-BiOBr nanosheets and BiOBr nanoplates, respectively. (f) EPR spectra of V_O-BiOBr nanosheets and BiOBr nanoplates at room temperature.

generation of abundant oxygen vacancies.[34,35] Moreover, PVP molecules could selectively interact with specific crystalline planes of BiOBr, which could significantly suppress the growth of {102} facets during the hydrothermal synthetic process, leading to the formation of V_O-BiOBr nanosheets with large area, ultrathin thickness, and major exposed facets of {001} crystalline planes. No obvious characteristic peaks from other phases or impurities were observed, confirming the high purity of the products. The specific surface areas of both samples were measured by nitrogen adsorption/desorption isotherms according to the Brunauer−Emmer−Teller (BET) model. As presented in Figure S1, the specific surface area of V_O-BiOBr nanosheets (19.3 $m^2 \cdot g^{-1}$) is comparable to that of BiOBr nanoplates (20.0 $m^2 \cdot g^{-1}$).

The surface compositions of the products were characterized by XPS analysis. The survey spectra of XPS (Figure 3b) confirmed the presence of Bi, O, and Br elements. The adventitious carbon signal at 284.6 eV was employed to calibrate the XPS peaks. To investigate the element valence status of the samples, corresponding high-resolution XPS scans (Figure 3c−e) were performed. For V_O-BiOBr nanosheets, the XPS spectrum at Bi 4f region (Figure 3c) shows two strong peaks located at 158.4 and 163.6 eV, which are assigned to Bi $4f_{7/2}$ and Bi $4f_{5/2}$ bands of the Bi^{3+} species, respectively. The other two weak peaks at 157.2 and 163.1 eV are indexed to Bi $4f_{7/2}$ and Bi $4f_{5/2}$ bands, which are originated from low valence state Bi species accompanied by oxygen vacancies. The Br 3d XPS spectrum of V_O-BiOBr nanosheets (Figure 3d) displays two peaks at 67.3 and 68.2 eV, assignable to Br $3d_{5/2}$ and Br $3d_{3/2}$, respectively. In contrast, the binding energies of Bi and Br elements in BiOBr nanoplates are higher than those of V_O-BiOBr nanosheets. In O 1s XPS spectrum of V_O-BiOBr nanosheets (Figure 3e), three peaks at 529.2, 530.6, and 531.9 eV are observed, which are attributed to the lattice oxygen (O^{2-}) of BiOBr, the oxygen atoms in the vicinity of oxygen vacancies, and the adsorbed O_2 molecules, respectively.[36−38] Compared to BiOBr nanoplates, the O 1s peak of the oxygen atoms close to the oxygen vacancies in V_O-BiOBr nanosheets is much stronger and down-shifted from 531.8 to 530.6 eV, indicating the presence of more oxygen defects in V_O-BiOBr nanosheets.

Electron paramagnetic resonance (EPR) spectra were further employed to identify the oxygen vacancies. As shown in Figure 3f, the EPR spectrum of V_O-BiOBr nanosheets shows a strong peak at 348 mT, confirming the presence of oxygen vacancies, whereas the EPR spectrum of BiOBr nanoplates shows almost no signal. According to the previous reports, oxygen vacancies can delocalize electrons and thus substantially prevent the recombination of photogenerated electrons and holes, beneficial to the photocatalytic processes.[39,40]

To investigate the effect of oxygen vacancies on the semiconductive and photocatalytic properties, further characterizations were performed on the V_O-BiOBr nanosheets and BiOBr nanoplates. UV−vis diffuse reflectance spectra (DRS) show that the absorption edge of V_O-BiOBr nanosheets is red-shifted to 470 nm (Figure 4a), which is 30 nm longer than the absorption edge of BiOBr nanoplates (440 nm). Moreover, compared to BiOBr nanoplates, the V_O-BiOBr nanosheets show a stronger light absorption capability in the visible range between 450−750 nm and also exhibit darker color (as shown in the insets of Figure 4a). The Tauc plots (Figure 4b) reveal the bandgap of V_O-BiOBr nanosheets (2.43 eV) is smaller than that of BiOBr nanoplates (2.69 eV). XPS valence band spectra were employed to further study the band structures of both samples. As shown in Figure 4c, compared to the VBM of BiOBr nanoplates (1.50 eV), the valence band maximum (VBM) of V_O-BiOBr nanosheets is shifted to 0.95 eV. According to the combined analysis of band positions based on the Tauc plots and XPS valence band spectra (Figure 4b,c), it can be concluded that the conduction band minimum (CBM) of V_O-BiOBr nanosheets is shifted to −1.48 eV, while the CBM of BiOBr nanoplates is −1.19 eV. The enhanced light absorption and up-shifted conduction band are beneficial to the photocatalytic performance. The differences of energy band positions between V_O-BiOBr nanosheets and BiOBr nanoplates is illustrated in Figure 4d. On the basis of the above analysis, the effect of oxygen vacancies to the photocatalytic nitrogen fixation on V_O-BiOBr nanosheets and BiOBr nanoplates can be deduced (Figure 4e). The photoinduced electrons in the V_O-BiOBr nanosheets are first captured by the oxygen vacancies and then participate in the nitrogen reduction reaction, thus facilitating the charge separation and promote the reaction rate. In contrast, the photoinduced electrons generated in the BiOBr nanoplates are directly used to react with N_2 and H_2O molecules, which may suffer from charge recombination.

Electrochemical impedance spectra (EIS) were used to investigate the charge transport properties and interfacial resistances of the samples (Figure 5a,b). For both V_O-BiOBr nanosheets and BiOBr nanoplates, the arc radii of Nyquist plots under illumination are smaller than those measured

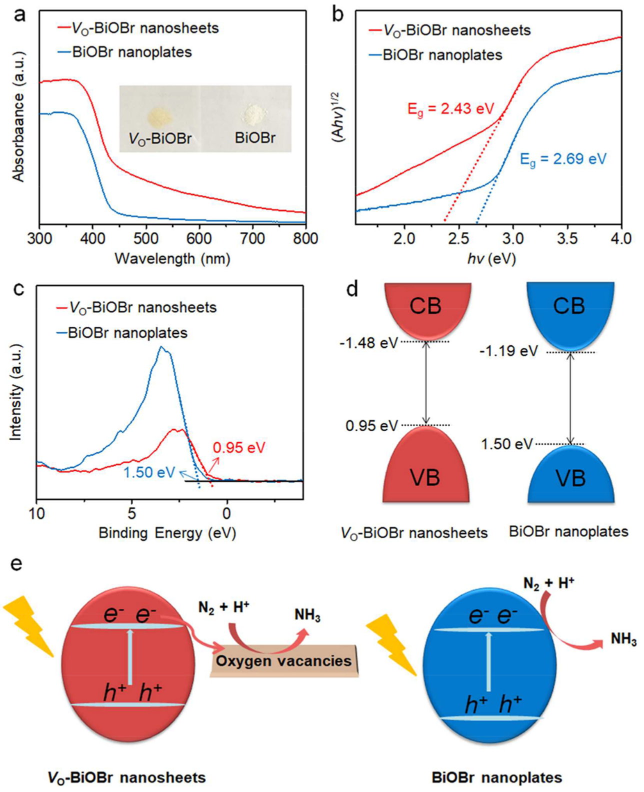

Figure 4. (a) UV−vis DRS curves of V_O-BiOBr nanosheets and BiOBr nanoplates. The insets show the color comparison of V_O-BiOBr nanosheets (left) and BiOBr nanoplates (right). (b) Corresponding Tauc ($(Ah\nu)^{1/2}$ versus $h\nu$) plots, (c) valence band XPS spectra and (d) band alignments of V_O-BiOBr nanosheets and BiOBr nanoplates, respectively. (e) Schematic illustration of photocatalytic ammonia synthesis process on V_O-BiOBr nanosheets and BiOBr nanoplates, respectively.

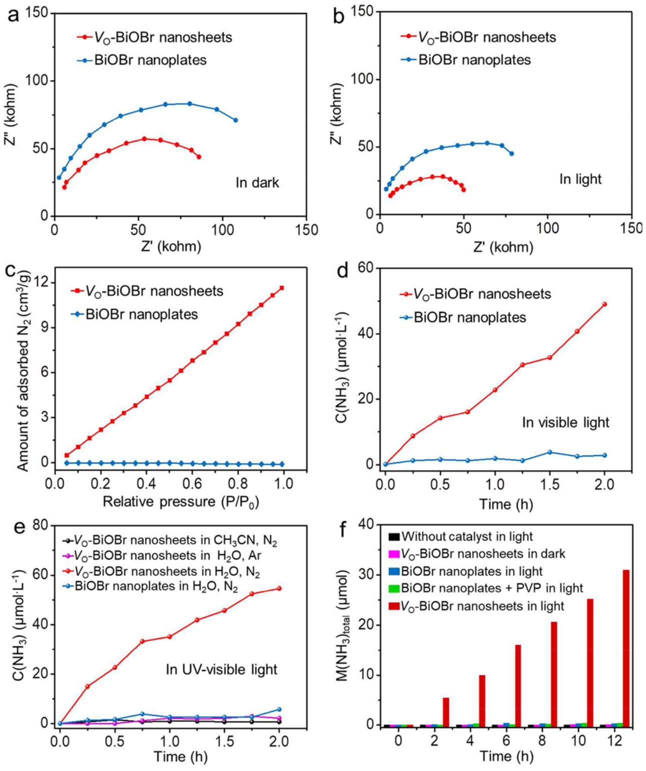

Figure 5. (a,b) Nyquist plots of V_O-BiOBr nanosheets and BiOBr nanoplates (a) in dark and (b) in light, respectively. (c) The N_2 adsorption isotherms V_O-BiOBr nanosheets and BiOBr nanoplates under room temperature. (d) The time curves of ammonia concentrations measured with V_O-BiOBr nanosheets and BiOBr nanoplates under the illumination of 300 W Xe lamp with 420 nm cutoff filter, respectively (50 mg photocatalyst + 100 mL ultrapure water). (e) Controlled experiments on photochemical N_2 fixation of V_O-BiOBr nanosheets and BiOBr nanoplates under different conditions and atmospheres with the full spectrum irradiation of 300 W Xe lamp (50 mg photocatalyst + 100 mL solvent). (f) The time histograms of ammonia concentrations obtained with different samples and test conditions.

under dark, owing to the abundant photoinduced electrons and holes on the catalysts generated under illumination. Notably, no matter under dark or under illumination, the arc radii of V_O-BiOBr nanosheets are smaller than those of BiOBr nanoplates, indicating the oxygen vacancies in V_O-BiOBr nanosheets can greatly promote charge transport and decrease the interfacial resistance.

To compare the nitrogen adsorption capability of V_O-BiOBr nanosheets and BiOBr nanoplates, volumetric N_2 adsorption measurements were performed under room temperature (Figure 5c). The result reveals that the V_O-BiOBr nanosheets are able to absorb N_2 molecules, while the BiOBr nanoplates can hardly absorb N_2 at mild conditions. DFT calculations also reveal the energetically unfavorable adsorption of N_2 molecule on BiOBr slab model without the oxygen vacancies, as detailed below. These result suggest that the introduction of oxygen vacancies is very conductive to the adsorption of inert N_2 molecules, which benefits to the reaction rate and conversion efficiency of nitrogen photofixation.

The photocatalytic nitrogen fixation activities of V_O-BiOBr nanosheets and BiOBr nanoplates were evaluated and compared. The concentration of generated ammonia was measured by Nessler's reagent colorimetric method and carefully calibrated (Figure S2). There is no ammonia detected in the absence of photocatalyst or light illumination, suggesting the photocatalyst and light illumination are essential to the nitrogen fixation. Under the visible-light illumination of 300 W Xe lamp with a 420 nm cutoff filter, the V_O-BiOBr nanosheets display a much higher photocatalytic activity for ammonia production than that of BiOBr nanoplates (Figure 5d). The V_O-BiOBr nanosheets show an average rate of photocatalytic ammonia generation of 49.04 $\mu mol \cdot g^{-1} \cdot h^{-1}$ within 2 h, while the average rate of photocatalytic ammonia generation of BiOBr nanoplates is only 2.83 $\mu mol \cdot g^{-1} \cdot h^{-1}$. Under the full-range light illumination without cutoff filter, the photocatalytic rate of V_O-BiOBr nanosheets and BiOBr nanoplates increased to 54.7 and 5.75 $\mu mol \cdot g^{-1} \cdot h^{-1}$, respectively.

To confirm the N source and the proton source of the produced NH_3 are originated from N_2 and H_2O, the controlled experiments of photochemical N_2 fixation reaction on *Vo*-BiOBr nanosheets under Ar atmosphere and in acetonitrile (CH_3CN) were conducted, respectively. As shown in Figure 5e, there was no ammonia detected on *Vo*-BiOBr nanosheets when N_2 and H_2O were replaced by Ar and CH_3CN, indicating that N_2 and H_2O were the N and proton sources of NH_3 production, respectively. In addition, to investigate the influence of adsorbed PVP, the photocatalytic nitrogen fixation activity of the mixture of BiOBr nanoplates and PVP was evaluated. As presented in Figure 5f, the addition of PVP has

DOI: 10.1021/acs.nanolett.8b03655
Nano Lett. 2018, 18, 7372−7377

almost no impact on photocatalytic performance of nitrogen fixation.

Besides, room-temperature EPR spectroscopy was performed to evaluate the relative concentrations of oxygen vacancies on *V*o-BiOBr nanosheets before and after the UV−visible light irradiation, respectively. As shown in Figure S3, the signal intensity of the EPR spectra shows almost no change before and after the UV−visible light irradiation, indicating that the Xe lamp irradiation without cutoff filter cannot produce more oxygen vacancies on *V*o-BiOBr nanosheets. In view of the identical chemical compositions and the comparable specific surface areas between V_O-BiOBr nanosheets and BiOBr nanoplates, it can be concluded that the oxygen vacancies generated during the synthesis process of V_O-BiOBr nanosheets are responsible for the significantly improved photocatalytic activity for nitrogen fixation.

As shown in Figure 5f, after working for 12 h under illumination (repeated 6 testing cycles for 2 h periods), the V_O-BiOBr nanosheets still well maintain the ability of photocatalytic N_2 fixation, delivering a total ammonia production amount of 30.9 μmmol and an average ammonia generation rate of 51.5 $\mu mmol \cdot g^{-1} \cdot h^{-1}$, indicating the good stability during the photocatalytic process. In addition, SEM and XRD characterizations (Figures S4 and S5) show that the morphology and crystalline structure of V_O-BiOBr nanosheets and BiOBr nanoplates remain almost unchanged after long-term testing, further confirming the well-preserved structural integrity of the BiOBr photocatalysts.

To understand the origins of enhanced photocatalytic N_2 fixation performance on V_O-BiOBr nanosheets, it is important to gain a fundamental insight into the role of oxygen vacancies in reaction mechanism through theoretical simulations. DFT calculations were carried out to investigate the possible reaction pathways of N_2 fixation on the V_O-BiOBr (001) surface with a slab model, as shown in Figure S6. For the N_2 fixation on the exposed V_O-BiOBr (001) surface, DFT calculations confirm that the reaction pathway favors the hydrogenation of distal N^1 atom ($N^2{\equiv}N^{1}*$), as indicated by the reaction steps 1−4 (Figure 6a). As confirmed by above studies, the rich oxygen vacancies on V_O-BiOBr are responsible for the N_2 adsorption and enhanced catalytic activity. Briefly, N_2 molecules are first absorbed on to the oxygen vacancies on the V_O-BiOBr (001) surface and activated at the reaction step 1, with the length of N≡N bond increases from 1.11 to1.24 Å (Figure 6b). The following step 2 is the key step of the hydrogenation of distal N^1 atom to yield N≡NH*, which is exergonic with an energy change of 1.40 eV (Figure 6c). The subsequent intermediate hydrogenation product at the step 3 is $N{\equiv}NH_2*$, associated with the reduction of N≡N bond to N═N bond. At the step 4, $N{=}NH_2*$ is further hydrogenated to generate an intermediate of $N{-}NH_3*$ with a single N—N bond length of 1.47 Å (Figure 6b), then an energy input of 1.07 eV is required to cleave the N—N bond (Figure 6c). This leads to the release of the first NH_3 molecule after the N—N bond splitting.[41] The subsequently formed three intermediates are NH*, NH_2*, and NH_3*, which were found to be also exergonic with the energy outputs of 3.34, 3.58, and 3.15 eV, respectively. Finally, the amine intermediate NH_3* requires another energy input of 1.03 eV to release the second NH_3 molecule. In contrast, for the N_2 fixation on the BiOBr (001) surface without oxygen vacancies, DFT calculation indicates that N_2 molecule is difficult to adsorb and activate on the BiOBr (001) surface, as evidenced by the increase of $O{-}N^1$ distance from 3.23 Å (step 1) to 3.63 Å (step 4) (Figure S7), which is consistent with the above experimental results. These calculation results indicate that the oxygen vacancies on V_O-BiOBr (001) surface are crucial to the N_2 fixation, which is conducive to the N_2 adsorption and formation of intermediates for ammonia production.

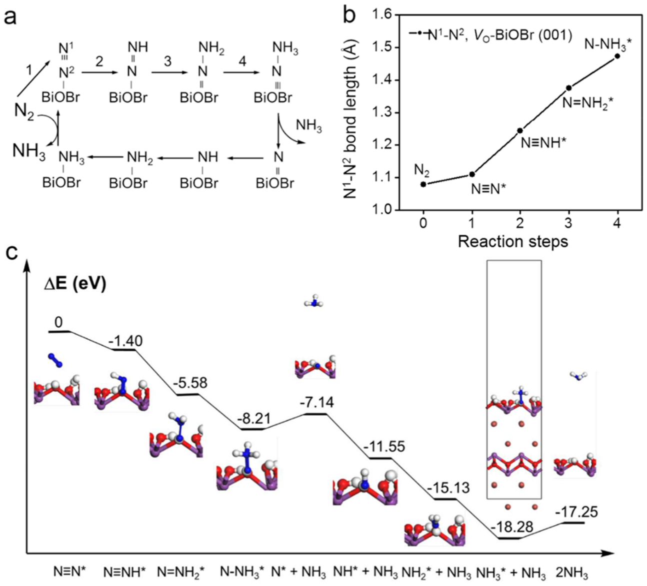

Figure 6. (a) Schematic reaction pathway of V_O-mediated N_2 fixation on V_O-BiOBr (001) surface with the distal mechanism of terminal end-on bound N_2. (b) The $N^1{-}N^2$ bond distance variation during the V_O-mediated N_2 fixation process on V_O-BiOBr (001) surface. (c) The energy change for the V_O-mediated N_2 fixation on V_O-BiOBr (001) surface.

In summary, here we demonstrate that the introduction of oxygen vacancies in BiOBr photocatalyst by the surfactant-assisted synthesis has great effect on the photocatalytic activity for nitrogen fixation. On the basis of detailed characterizations and tests, it is confirmed that the oxygen defects can enhance the light absorption, narrow the bandgap, and change the positions of conduction band and valence band. Moreover, the oxygen vacancies can effectively inhibit the recombination of photogenerated electrons and holes. DFT calculations indicate that the oxygen vacancies can facilitate the adsorption and activation of inert N_2 molecules. As a result, the photocatalytic activity of V_O-BiOBr nanosheets is much superior to that of BiOBr nanoplates without vacancies. This work points out a feasible way to design high-performance photocatalysts for solar-driven ammonia synthesis via the vacancy and defect engineering.

■ ASSOCIATED CONTENT

Ⓢ Supporting Information

The Supporting Information is available free of charge on the ACS Publications website at DOI: 10.1021/acs.nanolett.8b03655.

Table S1 and Figures S1−S7; synthetic, experimental and computational details, additional information including the calculated total energies of corresponding free and adsorbed molecules, nitrogen adsorption−desorption isotherms, the standard calibration curve for colorimetric NH_4^+ assay, EPR spectra, SEM images, XRD patterns, the simulated structures of V_O-BiOBr

(001) surface, the calculated energy change and the variation of O−N^1 distance, and schematic structure of N_2 molecule on the BiOBr (001) surface without oxygen vacancies. (PDF)

AUTHOR INFORMATION

Corresponding Author

*E-mail: zhongjin@nju.edu.cn. Phone: +86-18115605182.

ORCID

Jie Liu: 0000-0003-0451-6111

Jing Ma: 0000-0001-5848-9775

Zhong Jin: 0000-0001-8860-8579

Author Contributions

X.X., R.C., and H.C. contributed equally.

Notes

The authors declare no competing financial interest.

ACKNOWLEDGMENTS

This work was supported by National Key R&D Program of China (2017YFA0208200, 2016YFB0700600, 2015CB659300), Projects of NSFC (21872069, 51761135104, 21573108), Natural Science Foundation of Jiangsu Province (BK20180008, BK20150583, BK20160643), High-Level Entrepreneurial and Innovative Talents Program of Jiangsu Province, and the Fundamental Research Funds for the Central Universities of China (020514380146). We are also grateful to the High-Performance Computing Center of Nanjing University and Nanxin Pharm Co., Ltd., Nanjing, for the help of the quantum chemical calculations in this paper.

REFERENCES

(1) Rusina, O.; Linnik, O.; Eremenko, A.; Kisch, H. *Chem. - Eur. J.* **2003**, *9*, 561−565.

(2) Knobloch, D. J.; Lobkovsky, E.; Chirik, P. *Nat. Chem.* **2010**, *2*, 30−35.

(3) van der Ham, C. J. M.; Koper, M. T.; Hetterscheid, D. G. H. *Chem. Soc. Rev.* **2014**, *43*, 5183−5191.

(4) Kitano, M.; Inoue, Y.; Yamazaki, Y.; Hayashi, F.; Kanbara, S.; Matsuishi, S.; Yokoyama, T.; Kim, S.-W.; Hara, M.; Hosono. *Nat. Chem.* **2012**, *4*, 934−940.

(5) Lan, R.; Irvine, J. T. S.; Tao, S. *Sci. Rep.* **2013**, *3*, 1145.

(6) Zeng, H.; Terazono, S.; Tanuma, T. *Catal. Commun.* **2015**, *59*, 40−44.

(7) Tsuji, Y.; Kitano, M.; Kishida, K.; Sasase, M.; Yokoyama, T.; Hara, M.; Hosono, H. *Chem. Commun.* **2016**, *52*, 14369−14372.

(8) Tanaka, H.; Nishibayashi, Y.; Yoshizawa, K. *Acc. Chem. Res.* **2016**, *49*, 987−995.

(9) Bao, D.; Zhang, Q.; Meng, F. L.; Zhong, H. X.; Shi, M. M.; Zhang, Y.; Yan, J. M.; Jiang, Q.; Zhang, X. B. *Adv. Mater.* **2017**, *29*, 1604799.

(10) Liu, J.; Kelley, M. S.; Wu, W.; Banerjee, A.; Douvalis, A. P.; Wu, J.; Zhang, Y.; Schatz, G. C.; Kanatzidis, M. G. *Proc. Natl. Acad. Sci. U. S. A.* **2016**, *113*, 5530−5535.

(11) Banerjee, A.; Yuhas, B. D.; Margulies, E. A.; Zhang, Y.; Shim, Y.; Wasielewski, M. R.; Kanatzidis, M. G. *J. Am. Chem. Soc.* **2015**, *137*, 2030−2034.

(12) Schrauzer, G. N.; Guth, T. D. *J. Am. Chem. Soc.* **1977**, *99*, 7189−7193.

(13) Soria, J.; Conesa, J. C.; Augugliaro, V.; Palmisano, L.; Schiavello, M.; Sclafani, A. *J. Phys. Chem.* **1991**, *95*, 274−282.

(14) Boucher, D. L.; Davies, J. A.; Edwards, J. G.; Mennad, A. *J. Photochem. Photobiol., A* **1995**, *88*, 53−64.

(15) Ranjit, K. T.; Varadarajan, T. K.; Viswanathan, B. *J. Photochem. Photobiol., A* **1996**, *96*, 181−185.

(16) Jacobsen, C. J.; Dahl, S.; Hansen, P. L.; Törnqvist, E.; Jensen, L.; Topsøe, H.; Prip, D. V.; Møenshaug, P. B.; Chorkendorff, Ib. *J. Mol. Catal. A: Chem.* **2000**, *163*, 19−26.

(17) Rao, N. N.; Dube, S.; Natarajan, P. *Appl. Catal., B* **1994**, *5*, 33−42.

(18) Zhu, D.; Zhang, L.; Ruther, R. E.; Hamers, R. *Nat. Mater.* **2013**, *12*, 836−841.

(19) Christianson, J. R.; Zhu, D.; Hamers, R. J.; Schmidt, J. R. *J. Phys. Chem. B* **2014**, *118*, 195−203.

(20) Ji, Y.; Luo, Y. *J. Am. Chem. Soc.* **2016**, *138*, 15896−15902.

(21) Guan, M.; Xiao, C.; Zhang, J.; Fan, S.; An, R.; Cheng, Q.; Xie, J.; Zhou, M.; Ye, B.; Xie, Y. *J. Am. Chem. Soc.* **2013**, *135*, 10411−10417.

(22) Liu, Y.; Xiao, C.; Xie, Y. *Adv. Energy Mater.* **2016**, *6*, 1600436.

(23) Zhang, N.; Li, X.; Ye, H.; Chen, S.; Ju, H.; Liu, D.; Lin, Y.; Ye, W.; Wang, C.; Xu, Q.; Zhu, J.; Song, L.; Jiang, J.; Xiong, Y. *J. Am. Chem. Soc.* **2016**, *138*, 8928−8935.

(24) Rahman, M. A.; Bazargan, S.; Srivastava, S.; Wang, X.; Abd-Ellah, M.; Thomas, J. P.; Heinig, N. F.; Pradhan, D.; Leung, K. T. *Energy Environ. Sci.* **2015**, *8*, 3363−3373.

(25) Dong, G.; Ho, W.; Wang, C. *J. Mater. Chem. A* **2015**, *3*, 23435−23441.

(26) Wu, G.; Gao, Y.; Zheng, B. *Ceram. Int.* **2016**, *42*, 6985−6992.

(27) Li, H.; Shang, J.; Ai, Z.; Zhang, L. *J. Am. Chem. Soc.* **2015**, *137*, 6393−6399.

(28) Hu, S.; Chen, X.; Li, Q.; Zhao, Y.; Mao, W. *Catal. Sci. Technol.* **2016**, *6*, 5884−5890.

(29) Sun, S.; Li, X.; Wang, W.; Zhang, L.; Sun, X. *Appl. Catal., B* **2017**, *200*, 323−329.

(30) Zhang, X.; Ai, Z.; Jia, F.; Zhang, L. *J. Phys. Chem. C* **2008**, *112*, 747−753.

(31) Zhang, D.; Jing, L.; Wang, Q.; Wu, Q. *J. Mater. Chem. A* **2013**, *1*, 8622−8629.

(32) Li, H.; Liu, J.; Liang, X.; Hou, W.; Tao, X. *J. Mater. Chem. A* **2014**, *2*, 8926−8932.

(33) Wang, X.; Zhao, Y.; Li, F.; Dou, L.; Li, Y.; Zhao, J.; Hao, Y. *Sci. Rep.* **2016**, *6*, 24918.

(34) Zhang, G.; Hu, Z.; Sun, M.; Liu, Y.; Liu, L.; Liu, H.; Huang, C.; Qu, J.; Hong, J. *Adv. Funct. Mater.* **2015**, *25*, 3726−3734.

(35) Kavitha, M. K.; Jinesh, K. B.; Philip, R.; Gopinath, P.; John, H. *Phys. Chem. Chem. Phys.* **2014**, *16*, 25093−25100.

(36) Wang, J.; Wang, Z.; Huang, B.; Ma, Y.; Liu, Y.; Qin, X.; Zhang, X.; Dai, Y. *ACS Appl. Mater. Interfaces* **2012**, *4*, 4024−4030.

(37) Ye, L.; Zan, L.; Tian, L.; Peng, T.; Zhang, J. *Chem. Commun.* **2011**, *47*, 6951−6953.

(38) Gao, S.; Sun, Z.; Liu, W.; Jiao, X.; Zu, X.; Hu, Q.; Sun, Y.; Yao, T.; Zhang, W.; Wei, S.; Xie, Y. *Nat. Commun.* **2017**, *8*, 14503.

(39) Lei, F.; Sun, Y.; Liu, K.; Gao, S.; Liang, L.; Pan, B.; Xie, Y. *J. Am. Chem. Soc.* **2014**, *136*, 6826−6829.

(40) Ye, L.; Deng, K.; Xu, F.; Tian, L.; Peng, T.; Zan, L. *Phys. Chem. Chem. Phys.* **2012**, *14*, 82−85.

(41) Li, H.; Shang, J.; Shi, J.; Zhao, K.; Zhang, L. *Nanoscale* **2016**, *8*, 1986−1993.